Electric field control of spin waves in ultrathin CoFeB films

Bivas Rana,[1,*] Samiran Choudhury,[2] Katsuya Miura,[3] Hiromasa Takahashi,[3] Anjan Barman,[2] and YoshiChika Otani[1,4,†]

[1]*Center for Emergent Matter Science, RIKEN, 2-1 Hirosawa, Wako 351-0198, Japan*

[2]*Department of Condensed Matter Physics and Material Sciences, S. N. Bose National Centre for Basic Sciences, Block JD, Sector III, Salt Lake, Kolkata 700 106, India*

[3]*Research and Development Group, Hitachi, Ltd., 1–280 Higashi-koigakubo, Kokubunji-shi, Tokyo 185–8601, Japan*

[4]*Institute for Solid State Physics, University of Tokyo, Kashiwa 277–8581, Japan*

(Received 10 March 2019; revised manuscript received 23 September 2019; published 13 December 2019)

Recently, investigation and control of the properties of propagating spin waves (SWs) in ultrathin ferromagnetic films have attracted considerable attention because of their possible technological impact on future nanoscale magnonic devices. Control of SW properties using voltage-controlled magnetic anisotropy (VCMA) may reduce the power consumption of future magnonic devices significantly. Here, we report an experimental study of manipulation of uniform ferromagnetic resonance (UFMR) and dipole-exchange SWs by VCMA in ultrathin $Co_{20}Fe_{60}B_{20}$ (CoFeB) films with thicknesses of 1.6, 1.8, and 2.0 nm. The UFMR and the SWs are excited using microwave antennae and detected by spin pumping and inverse spin Hall effect techniques. A significant change in the SW frequency caused by VCMA is observed, particularly in the 1.6-nm-thick CoFeB film, where the effective value of the net anisotropy is quite small because of the presence of strong interfacial perpendicular magnetic anisotropy. Additionally, micromagnetic simulations are performed to demonstrate that the SWs in the 1.6-nm-thick CoFeB film with its in-plane easy axis of magnetization can be guided through virtual nanochannels formed by VCMA.

DOI: 10.1103/PhysRevB.100.224412

I. INTRODUCTION

Perturbations created in ordered magnetic materials can set off waves known as spin waves (SWs) [1–4] that can travel through the magnetic materials and carry information with significantly low power consumption. The SWs, i.e., magnons (the particle counterpart of SWs) have been the center of attention in research fields known as magnonics [5,6] and magnon spintronics [7], which is the magnetic analog of photonics. Various types of magnonic devices, including oscillators, filters, attenuators, switches, multiplexers, logic gates, transistors, and converters, based on SWs have been proposed in the literature. Recently, it was proposed that electric field modulation of the interfacial perpendicular magnetic anisotropy (iPMA) would provide an excellent method for development of ultralow-power nanoscale magnonic devices [8–12]. Perpendicular magnetic anisotropy (PMA) has been observed at the interfaces between 3*d* transition metal ferromagnetic materials (e.g., Fe, CoFeB) and nonmagnetic insulators (e.g., MgO, Al_2O_3) as a result of hybridization of the out-of-plane 3*d* orbitals of the ferromagnetic (FM) material and the out-of-plane 2*p* orbital of oxygen [13–16]. When an electric field is applied at the FM/oxide interface, it causes a change in the number of electrons in the out-of-plane 3*d* orbitals of Fe with respect to the in-plane orbitals, as indicated by first principles calculations [17,18]. The relative change in the electronic occupation state modifies the bonding strength of the 3*d*-2*p* orbitals, which then modulates iPMA through spin-orbit coupling (SOC) of the FMs [16,17,19].

Nozaki *et al.* [8] and Zhu *et al.* [20] showed that voltage-controlled magnetic anisotropy (VCMA) can excite uniform ferromagnetic resonance (UFMR) efficiently with ultralow power consumption. A number of reports were published subsequently, which revealed that VCMA is also an excellent tool for excitation of both linear [9] and nonlinear [21–23] SWs and nonlinear ferromagnetic resonance [23]. After excitation, the SWs need to be guided through a channel to ensure that they reach the target position on the spin wave waveguide (SWWG). Rana *et al.* proposed that SWs can be guided through reconfigurable nanochannels formed by VCMA [11]. Recently, directional channeling of SWs was proposed by controlling the SW phase using VCMA [24]. It is also important to be able to manipulate the SW properties, including frequency, wave vector, propagation length, group velocity, and dispersion characteristics, i.e., the magnonic band structures, to enable the development of a variety of magnonic devices. Nagaoka *et al.* showed that the resonance fields of propagating magnetostatic surface spin waves in relatively thick FM films with iPMA can be controlled using VCMA without a charge current [25]. Because a thicker FM film was used as the SWWG, the change in the resonance field was quite small. In their report, the SWs were excited and detected using microwave antennae through an inductive coupling process. Unfortunately, this detection method is very inefficient for ultrathin FM films because of the reduced volume of the FM material. Very recently, it was shown that spin pumping and the ensuing inverse spin Hall effect (ISHE) could provide an alternative method for electrical detection

*bivas.rana@riken.jp, bivasranaiitd@gmail.com

†yotani@riken.jp

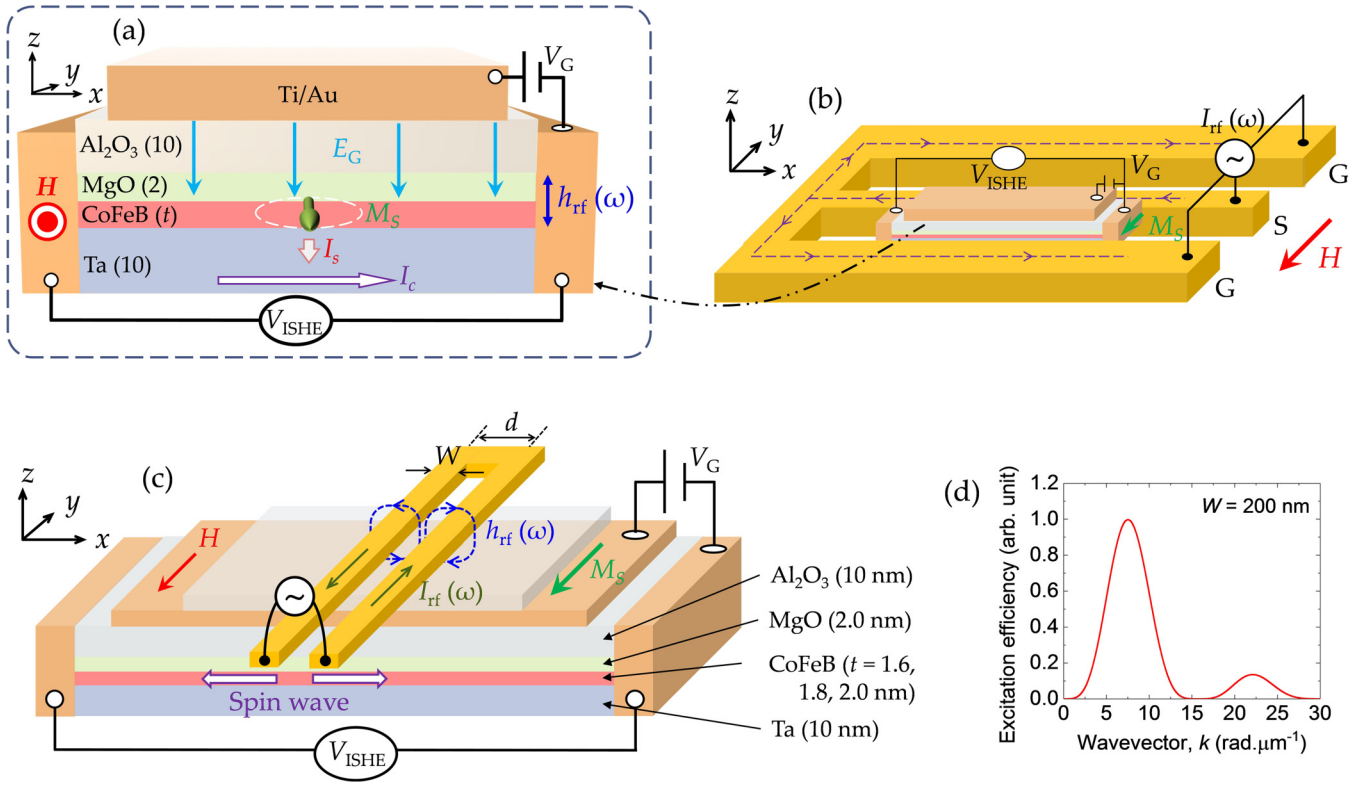

FIG. 1. (a) Schematic diagram showing the device structure details for the UFMR study and the mechanism for ISHE detection of the resonance signal under application of a DC gate voltage (V_G). (b) Schematic illustration of the experimental setup used for the UFMR measurements. A radio-frequency current (I_{rf}) is passed through a micrometer-sized antenna that surrounds the rectangular-shaped multilayer film. The I_{rf}-induced Oersted field (h_{rf}) excites the UFMR in the CoFeB film under the resonance conditions given by Eq. (2). (c) Schematic diagram of a rectangular shaped multilayer film with a nanoscale microwave antenna on top of it. A radio frequency current (I_{rf}) is passed through a microwave antenna to excite the SWs in the CoFeB film. A DC gate voltage (V_G) is applied across the top gate electrode and the CoFeB film to tune the SW frequency. (d) Calculated excitation efficiency of the SWs as a function of the SW wave vector (k).

of SWs in ultrathin FM films [26]. Although this is not a local detection technique, it can nevertheless be very useful for study of the resonance fields and frequencies of the SWs. In this experimental study, we demonstrate manipulation of the UFMR and the dipole-exchange SW frequency in ultrathin $Co_{20}Fe_{60}B_{20}$ (CoFeB) films. The UFMR and the SWs are excited using a microwave antenna (i.e., using a charge current induced Oersted field) and are detected via spin pumping and ISHE techniques. Furthermore, we perform numerical micromagnetic simulations to demonstrate that the SWs in ultrathin FM films with their lower effective net anisotropy values can be guided through virtual nanochannels formed by VCMA.

II. SAMPLE FABRICATION AND EXPERIMENTAL METHODS

The samples were fabricated for our study using a multistep fabrication method. A detailed description of the sample fabrication procedure can be found in Ref. [27]. First, multilayer stacks were deposited on $Si(001)/SiO_2(700\,nm)$ substrates by radio-frequency (RF) sputtering at room temperature and at a base pressure of about 10^{-8} Torr. These multilayer stacks consist of the following layer structure: $Si/SiO_2/Ta(10)/Co_{20}Fe_{60}B_{20}(t = 1.6,\ 1.8,\ 2.0)/MgO(2)/Al_2O_3(10)$, where the numbers in parentheses represent the nominal thicknesses of the corresponding layers in nanometers. These sputter-deposited films were then annealed at 280 °C in a vacuum under a perpendicular magnetic field of 600 mT for 1 h. The UFMR and SW measurement devices were then prepared from the annealed multilayer stacks using a combination of maskless ultraviolet photolithography, electron beam lithography, Ar^+ ion milling, RF magnetron sputtering and electron beam evaporation.

Initially, we study the UFMR to characterize the iPMA, the VCMA coefficient, and the damping parameters of the CoFeB films used in this work. Figure 1(a) shows a schematic diagram of a representative measurement device and the principle behind the UFMR measurements. Figure 1(b) shows a schematic diagram of the experimental setup used for the UFMR measurements. A signal generator is used to send an RF current (I_{rf}) through the micrometer-sized antenna that surrounds the rectangular-shaped ($100\,\mu m \times 10\,\mu m$) magnetic structure [Fig. 1(b)]. When the RF current passes through the antenna, it generates a microwave magnetic field (h_{rf}) oriented perpendicular to the film plane and thus excites the UFMR. To obtain the highest possible signal through the ISHE, the magnetizations of the FM films are oriented along the short axis of the rectangular structures (i.e., along the y axis) by application of a bias magnetic field (H) from an electromagnet [28]. For the UFMR study, H is swept from -175 to $+175$ mT in 0.5 mT steps while maintaining a constant RF signal frequency. When H satisfies the resonance condition [given

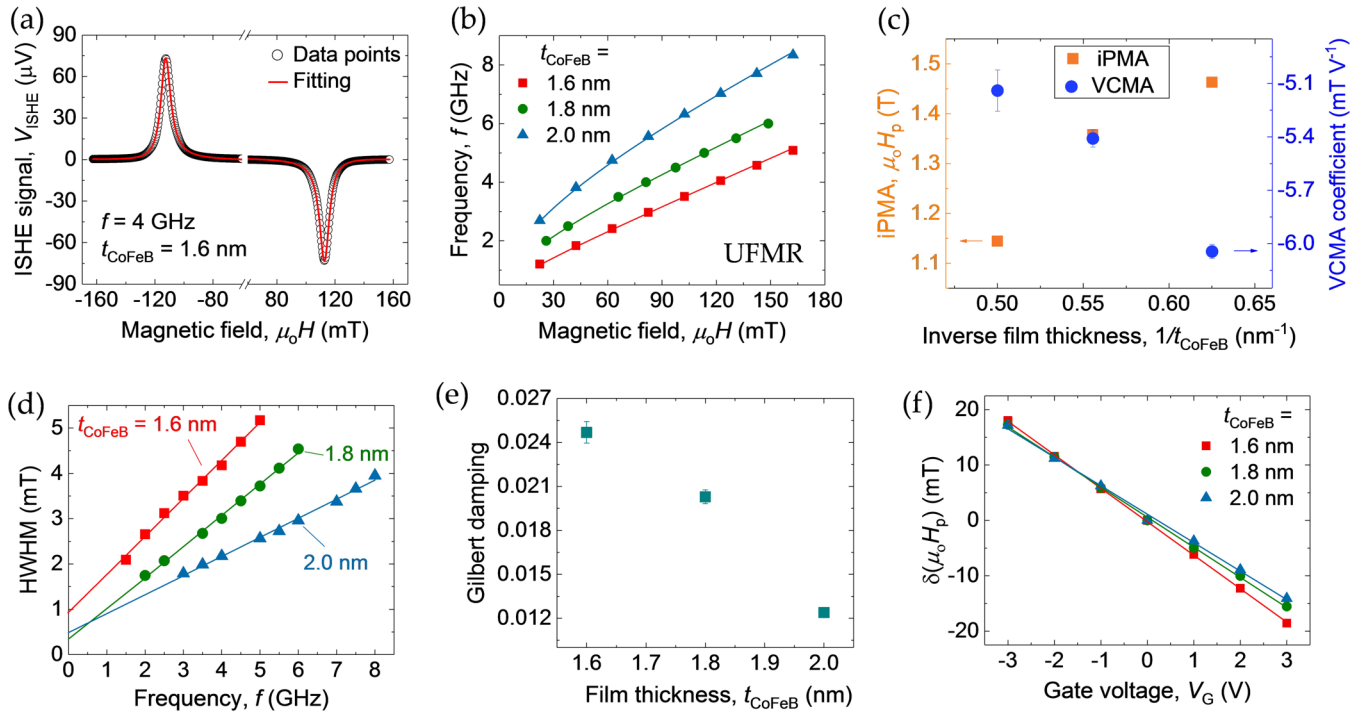

FIG. 2. (a) Measured ISHE signal corresponding to the UFMR of a 1.6-nm-thick CoFeB film at a microwave frequency of 4.0 GHz is plotted as a function of the bias magnetic field. The solid curve represents the fitting with Eq. (1). (b) UFMR frequencies of three different CoFeB films plotted as functions of the bias magnetic field. The solid curves represent the fittings using the Kittel formula described in Eq. (2). (c) Extracted iPMA field and VCMA coefficient values plotted as functions of the inverse of the CoFeB film thickness. (d) Extracted HWHM values plotted as a function of frequency. The solid lines represent fittings using a linear function. (e) Extracted Gilbert damping parameter values plotted as a function of the CoFeB film thickness (t_{CoFeB}). (f) Changes in the iPMA fields as a function of the gate voltage plotted for three different CoFeB film thicknesses. The solid lines represent fittings using a linear function.

as Eq. (2)], the UFMR amplitude of the CoFeB layer is significantly enhanced, and this pumps a pure spin current (I_s) into the adjacent Ta layer [Fig. 1(a)]. The pure spin current is then converted into a transverse charge current (I_c) by the ISHE of the Ta layer and the corresponding signal is acquired by measuring the potential drop (V_{ISHE}) across the Ta layer using a nanovoltmeter. Some UFMR measurements were also performed by sweeping the RF signal frequency in 20 MHz steps at a fixed value of H. To study the propagating SWs, I_{rf} is passed through a microwave antenna [Fig. 1(c)], while the magnetization is oriented along the short axis (i.e., the y axis) of the rectangular structure by application of a bias magnetic field H using an electromagnet. During these measurements, H remains constant, while the microwave signal frequency is swept from 1 to 10 GHz in 20 MHz steps. The SW signals are acquired by measuring the ISHE voltage (V_{ISHE}) across the rectangular structure, as shown in Fig. 1(c). To study the electric-field-based control of the UFMR and the SWs, a DC gate voltage (V_G) is applied across the top metal gate electrode and the CoFeB layer using a DC power source. This gate voltage produces the uniform electric field E_G at the CoFeB/MgO interface and modulates the iPMA.

III. RESULTS

A. Study of uniform ferromagnetic resonance from CoFeB films

Figure 2(a) shows an example of a measured ISHE signal corresponding to the UFMR of a 1.6-nm-thick CoFeB film at an applied microwave frequency $f = 4.0$ GHz. The opposite signs of the ISHE signals for opposite polarities of H confirms that the signal originates from the combination of spin pumping and ISHE [29]. To extract the resonance field (H_0), the resonance linewidth and the signal amplitude, the ISHE signals (denoted by V_{ISHE}) are fitted using a mathematical expression, where V_{ISHE} is written as a linear combination of symmetric and antisymmetric Lorentzian functions given by [30,31]

$$V_{ISHE} = C + \frac{V_s}{1 + (H - H_0)^2/\sigma^2} + \frac{V_a(H - H_0)/\sigma}{1 + (H - H_0)^2/\sigma^2}. \quad (1)$$

Here, C is the DC background of the ISHE signal, V_s and V_a are the weights of the symmetric and antisymmetric Lorentzian functions, respectively, and σ is the half width at half maximum (HWHM) of the resonance spectrum. The fitted curve is represented by the solid line in Fig. 2(a). The resonance spectrum appears to have a perfectly symmetrical Lorentzian shape. In Fig. 2(b), the UFMR frequencies (f_{UFMR}) are plotted as a function of H for CoFeB films of three different thicknesses. The iPMA values are extracted by fitting f_{UFMR} versus the H data points [represented by the solid curves in Fig. 2(b)] using the analytical Kittel formula given by [9,32]

$$f_{UFMR} = \left(\frac{\mu_0 \gamma}{2\pi}\right)[H(H + M_s - H_p(V_G))]^{1/2}, \quad (2)$$

where γ is the gyromagnetic ratio, H_p is the iPMA field, and M_s is the saturation magnetization. We used $\gamma = 29.4\,\mathrm{GHz\,T^{-1}}$ from Refs. [9,11] and $\mu_0 M_s = 1.5\,\mathrm{T}$ as obtained from vibrating sample magnetometer (VSM) measurements [27], while setting $\mu_0 H_p$ as a free parameter for fitting. The extracted $\mu_0 H_p$ values were 1.463, 1.358, and 1.144 T for CoFeB thickness (t_{CoFeB}) values of 1.6, 1.8, and 2.0 nm, respectively, as plotted in Fig. 2(c). The reduction in $\mu_0 H_p$ with increasing t_{CoFeB} confirms the interfacial origin of the PMA. Because $\mu_0 M_s > \mu_0 H_p$ in all the CoFeB films, the easy axis of magnetization therefore lies in the plane of the film in each case. This is further confirmed by anomalous Hall effect (AHE) measurements, as shown in Ref. [27]

To evaluate the Gilbert damping parameter (α), which originated from the bulk SOC of CoFeB and from spin pumping into Ta layer, the HWHM values of the resonance curves are plotted as a function of f [Fig. 2(d)] and are fitted using a linear function. Values of α are extracted from the slopes (Δ) of these linear fittings using the following expression [31,33]:

$$\alpha = \frac{\gamma}{2\pi}\Delta. \tag{3}$$

Figure 2(e) shows a plot of α as a function of t_{CoFeB}, which shows that the Gilbert damping parameter increases monotonically from 0.0124 to 0.0247 as the CoFeB thickness decreases from 2.0 to 1.6 nm. The Gilbert damping constants of our CoFeB films are slightly higher than previous reported values; that is probably due to the different qualities of the CoFeB and Ta films used in our case (which affect the bulk SOC of CoFeB and the spin Hall angle of Ta, respectively) [34]. Further detailed studies will be required to determine the exact reasons for the differences, but this lies outside the scope of the current study. The enhancement of the damping that occurs for thinner films is due to increments in the spin pumping contribution, as reported previously [34–36].

To evaluate the VCMA coefficients, i.e., the change in iPMA per unit gate voltage (V_G), we measured the UFMR signals of the CoFeB films for various values of V_G. Here, a positive gate voltage means that the top gate electrode has a positive potential with respect to the CoFeB film, which is used as the bottom electrode. We fitted the resonance spectra using Eq. (1) to determine the resonance field for each value of V_G and then calculated the anisotropy field ($\mu_0 H_p$) using Eq. (2). In Fig. 2(f), the changes in $\mu_0 H_p$ are plotted as a function of V_G for the different values of t_{CoFeB}. The results show that the iPMA varies linearly with V_G and that the slope of linear variation gives the value of the VCMA coefficient. The extracted VCMA coefficient values are -6.04, -5.41, and $-5.14\,\mathrm{mT\ V^{-1}}$ for $t_{\mathrm{CoFeB}} = 1.6$, 1.8, and 2.0 nm, respectively, as plotted in Fig. 2(c). Alternatively, by defining the VCMA coefficient as the change in the iPMA energy per unit surface area per unit applied electric field, the VCMA coefficient values for these three CoFeB films are all found to be $-70\,\mathrm{fJ\,V^{-1}\,m^{-1}}$.

B. ISHE detection of spin waves without gate voltage

Next, we study the nanoscale microwave antenna-induced propagating SW signals. We designed microwave antennae with two parallel arms with the same width (W) of 200 nm and an edge-to-edge separation of 200 nm, as shown schematically in Fig. 1(c). The center-to-center separation (d) of the arms of the antenna is 400 nm. The Fourier transform of the current distribution through the antenna gives the SW excitation efficiency for various values of the SW wave vector k [37]. In Fig. 1(d), the calculated efficiency of SW excitation by the designed antenna is plotted as a function of k, which indicates that the antenna excites SWs with maximum efficiency at a wave vector $k = 7.55\,\mathrm{rad\,\mu m^{-1}}$, i.e., at the wavelength $\lambda = 832\,\mathrm{nm}$. We neglect the second peak that appears at $k = 22\,\mathrm{rad\,\mu m^{-1}}$ here, because the excitation efficiency for this wave vector is reduced to approximately 14% when compared with the primary wave vector. The primary peak position can be estimated roughly to be $k = \pi/d$, where d is the center-to-center distance between the arms of the antenna. Because the excited SWs are governed by the dipole and exchange interactions under the present measurement conditions, these SWs can be called dipole-exchange SWs. The frequency (f_{SW}) versus wave vector (k) dispersion characteristics of these SWs can be expressed using an approximate analytical formula given in the literature [32,38]:

$$f_{\mathrm{SW}} = \left(\frac{\mu_0\gamma}{2\pi}\right)\left[\left(H + \frac{2A}{\mu_0 M_s}k^2\right)\left(H + \frac{2A}{\mu_0 M_s}k^2 + M_s - H_p(V_G)\right) + \frac{1}{4}M_s\{M_s - H_p(V_G)\}(1 - e^{-2kt_{\mathrm{CoFeB}}})\right]^{1/2}. \tag{4}$$

Here, A is the exchange stiffness constant. In Fig. 3(a), the calculated frequency (f_{SW}) versus wave vector (k) dispersion curves of the dipole-exchange SWs at $\mu_0 H = 60\,\mathrm{mT}$ are plotted for the CoFeB films with the three different thicknesses using the γ value of $29.4\,\mathrm{GHz\,T^{-1}}$ from Refs. [9,11], the $\mu_0 M_s$ value of 1.5 T from the VSM measurements [27], and the H_p value extracted from the UFMR measurements. The value of A is assumed to be $20\,\mathrm{pJ\,m^{-1}}$ [11,39]. The dotted horizontal lines represent the frequencies of the UFMR modes ($k = 0$), while the points at which the solid vertical line crosses the dispersion curves give the calculated frequencies of the SWs at $k = 7.55\,\mathrm{rad\,\mu m^{-1}}$. The measured SW signals from the three different CoFeB films are plotted in Fig. 3(b) (solid unfilled curves), along with the UFMR signals (filled curves). We then plot the frequencies of these UFMR modes and the SWs in Fig. 3(a). Although the measured frequency values of the UFMR modes match the analytical values perfectly, as expected, the SW frequency values show some discrepancies with respect to the analytical values. There are several possible reasons for these discrepancies. A small inhomogeneity in the bias magnetic field generated by the electromagnet and the inhomogeneous distribution of the iPMA across the CoFeB films may contribute to small changes in the measured values of the SW frequencies with respect to the calculated values. The real value of k may also differ from the calculated value because of slight deviations in the antenna dimensions from the nominal values. However, a small deviation in the antenna dimensions is unlikely to

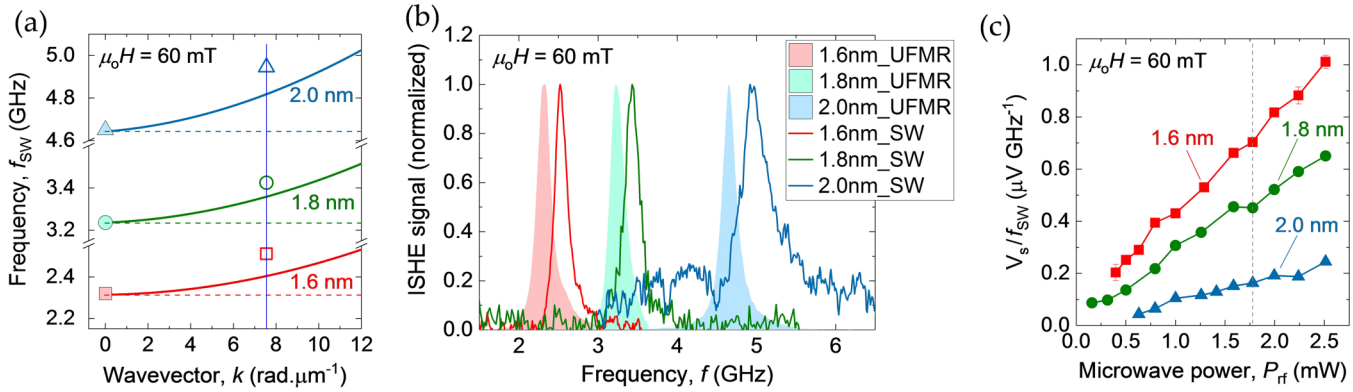

FIG. 3. (a) Calculated frequency versus wave vector dispersion curves of SWs plotted at $\mu_0 H = 60$ mT for $t_{CoFeB} = 1.6$, 1.8, and 2.0 nm. The dotted horizontal lines represent the calculated frequencies of the UFMR modes, i.e., the $k = 0$ modes. The crossing points of the solid vertical line with the dispersion curves give the expected numerical values for the SW frequencies at $k = 7.55\,\text{rad}\,\mu\text{m}^{-1}$. The measured frequencies of the UFMR mode and the SWs are represented by the filled and open symbols, respectively. (b) Experimentally measured ISHE signals, corresponding to the SWs, for three CoFeB films (solid unfilled curves). The measured UFMR signals are also represented by the filled curves. (c) Amplitudes of the measured ISHE signals of the SWs, which are normalized with respect to their corresponding resonance frequencies, plotted as a function of the microwave power (P_{rf}) applied to the antenna. The vertical dotted line represents the P_{rf} value used for the SW study.

produce a large discrepancy because of the weak dispersion of the SWs. We think that the difference between the adopted and the real values of exchange stiffness constant provides the dominant contribution to the observed discrepancies.

In this study, the group velocity (v_g) and the decay length (L_d) of the SWs cannot be measured directly in the experiments. However, their values can be estimated theoretically. The SW group velocity v_g can be calculated using the formula $v_g = 2\pi df/dk$, where df/dk is the slope of the dispersion curve. By calculating the slopes of the dispersion curves in Fig. 3(a) at $k = 7.55\,\text{rad}\,\mu\text{m}^{-1}$, the group velocities of the SWs for the CoFeB films with $t_{CoFeB} = 1.6$, 1.8, and 2.0 nm are estimated to be 142, 178, and 240 m s^{-1}, respectively. The SW decay length L_d can be expressed as $L_d = v_g/\Gamma$, where Γ is the relaxation rate given by [26]

$$\Gamma = 2\pi\alpha\gamma\mu_0\left[H + \frac{2A}{\mu_0 M_s}k^2 + \frac{1}{2}\left(M_s - H_p(V_G)\right)\right]. \quad (5)$$

The calculated L_d values for $t_{CoFeB} = 1.6$, 1.8, and 2.0 nm are 383, 355, and 436 nm, respectively. This shows that the SWs decay within a very short distance when compared with the excitation area, i.e., the lateral dimension of the antenna, which is ~ 600 nm. The reasons for this short decay length are the low v_g value and the high Γ value. The higher value of Γ in this case is due to the higher value of the damping constant α.

Next, we study the ISHE signal as a function of the microwave power. In the UFMR measurement case, the measured ISHE signal can be written as $V_{ISHE} \propto J_s \Theta_a R$, where J_s is the spin current density pumped into the heavy metal (which is Ta in our case), Θ_a is the spin Hall angle of Ta, and R is the resistance of the rectangular stack structure, i.e., the Ta/CoFeB/MgO/Al_2O_3 structure. The spin current density can be expressed as $J_s \propto f_{UFMR}\sin^2\theta$, where θ is the cone angle of magnetization precession [40]. We verified that the resistance (R) values of the rectangular stack structures, i.e., the Ta/CoFeB/MgO/Al_2O_3 structures, for devices with $t_{CoFeB} = 1.6$, 1.8, and 2.0 nm are almost identical. The spin Hall angle Θ_a of the Ta layer should also be the same for all devices because the films were deposited at the same time under identical conditions. Therefore, the measured ISHE signal V_{ISHE} should be proportional to $f_{UFMR}\sin^2\theta$. Within the limit of a small cone angle of precession, i.e., in the linear excitation regime, $\sin^2\theta$ can be approximated as θ^2, which is again proportional to the UFMR intensity (I_{ISHE}). Ultimately, we obtain the relationship $V_{ISHE} \propto f_{UFMR} I_{UFMR}$. A similar relationship can be obtained for SWs in the linear excitation regime given by $V_{ISHE} \propto f_{SW} I_{SW}$. Here, I_{SW} is the average SW intensity value. This shows that V_{ISHE}/f_{SW}, i.e., V_s/f_{SW}, is directly proportional to the SW intensity. Previous reports showed that the SW intensity I_{SW} is also proportional to the microwave power P_{rf} in the linear excitation regime [9], similar to the UFMR [41]. Here, we measured the SW signals (V_{ISHE}) as a function of P_{rf} from the three CoFeB films with varying thicknesses. In Fig. 3(c) we plot the amplitudes of the ISHE signals (V_s) corresponding to these SWs, normalized with respect to the resonance frequency (f_{SW}), as a function of P_{rf}. The plot shows that the frequency-normalized amplitudes of each of the ISHE signals, i.e., V_s/f_{SW}, increases linearly with increasing P_{rf} up to at least 2.5 mW, i.e., ~4 dBm. This verifies that the SWs are excited in the linear regime. The vertical dotted line represents the power (1.58 mW, i.e., ~2 dBm) used in our SW measurements. Interestingly, the value of V_s/f_{SW} increases monotonically with decreasing CoFeB thickness at the same P_{rf} magnitude. This means that the SW intensity for the 1.6-nm-thick CoFeB film has maximum value among the three CoFeB films because of the very weak value of its effective net anisotropy field, as determined from the UFMR measurements.

C. Electric field control of spin wave frequency and spin wave channeling

Next, we measured the SW signals for various gate voltage (V_G) values under a bias magnetic field of 60 mT. The measured ISHE signals are plotted in Figs. 4(a), 4(c), and

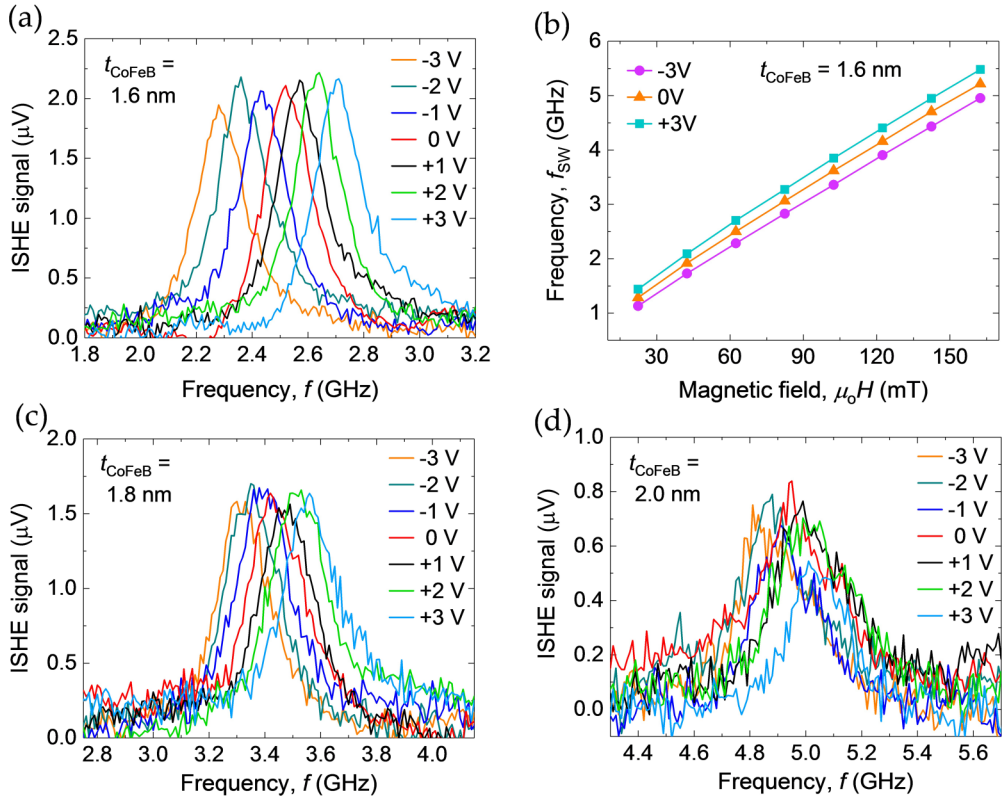

FIG. 4. ISHE signals of the SWs, measured at various values of gate voltage V_G and plotted for CoFeB films with (a) $t_{CoFeB} = 1.6$ nm, (c) 1.8 nm, and (d) 2.0 nm. (b) Measured SW frequencies from the CoFeB film with $t_{CoFeB} = 1.6$ nm plotted as a function of the bias magnetic field for three values of V_G.

4(d). The signal-to-noise ratio for the 1.6-nm-thick CoFeB film is much higher than the ratios for the 1.8 and 2.0 nm films because it produces a higher SW intensity for the same excitation power, as mentioned in the previous section. Furthermore, the change in the SW frequency with variation in V_G for the $t_{CoFeB} = 1.6$ nm film is also much higher than that for the other films. For example, the SW frequency (f_{SW}) of the $t_{CoFeB} = 1.6$ nm film is 2.520 GHz at $V_G = 0$ V, whereas $f_{SW} = 2.705$ and 2.280 GHz at $V_G = \pm 3$ V, respectively. Therefore, the average change in f_{SW} is approximately 210 MHz at $|V_G| = 3$ V, while the full width at half maximum (FWHM) of the resonance curve is approximately 200 MHz. In the cases of the CoFeB films with $t_{CoFeB} = 1.8$ and 2.0 nm, the changes in f_{SW} at $|V_G| = 3$ V are approximately 120 and 75 MHz, while the corresponding FWHM values are approximately 245 and 315 MHz, respectively. Because the change in f_{SW} with variation in V_G is higher than the resonance linewidth for the $t_{CoFeB} = 1.6$ nm film, this film can be used to confine the SWs inside the virtual nanochannels (NCs) formed by VCMA, as will be demonstrated below. We also measured f_{SW} as a function of the bias magnetic field $\mu_0 H$ at $V_G = 0$V, ± 3 V for the CoFeB films with $t_{CoFeB} = 1.6$, 1.8, and 2.0 nm. Representative results are shown for the $t_{CoFeB} = 1.6$ nm film in Fig. 4(b). The results for other films are shown in Ref. [27].

Previously, we have reported the confinement of exchange-dominated magnetostatic forward volume waves in virtual NCs formed using VCMA [11]. In that report, the easy axis of magnetization was out of the plane of the CoFeB film because of the strong iPMA (i.e., $\mu_0 H_p > \mu_0 M_s$). Here, we perform micromagnetic simulations to demonstrate the possibility of guiding dipole-exchange SWs through NCs that are formed using VCMA on an ultrathin FM film with in-plane orientation of the static magnetization. To demonstrate this possibility, we performed micromagnetic simulations using Object Oriented Micromagnetic Frameworks (OOMMF) software [42]. The details of the simulation procedure can be found in Refs. [11,27]. In this simulation, we selected a rectangular-shaped CoFeB film with dimensions of 2 μm (x) × 800 nm (y) × 1.6 nm (z). The iPMA field $\mu_0 H_p$ of this film is taken to be 1.463 T from the UFMR measurements of the CoFeB film with $t_{CoFeB} = 1.6$ nm. We assume that an NC with dimensions of 2 μm (x) × 200 nm (y) is formed along the middle of the rectangular-shaped film by application of $V_G = -3$ V. In practice, this type of NC can be formed by placing a metal gate electrode with dimensions of 2 μm (x) × 200 nm (y) on top of the oxide layer of the CoFeB film and applying a voltage across the gate electrode and the CoFeB film, as shown schematically in Fig. 5(a). When the VCMA coefficient of -6.05 mT V^{-1} from the UFMR measurement is adopted, the iPMA field of the NC becomes 1.482 T, while the field on the outside of the NC remains at 1.463 T. All other parameters, including γ, M_s, and A, are adopted from the UFMR measurement results. Here, we demonstrate the confinement of the dipole-exchange SWs under an in-plane bias magnetic field of $\mu_0 H = 160$ mT. The relatively higher bias magnetic field was selected to ensure that the static magnetization becomes uniform even at the

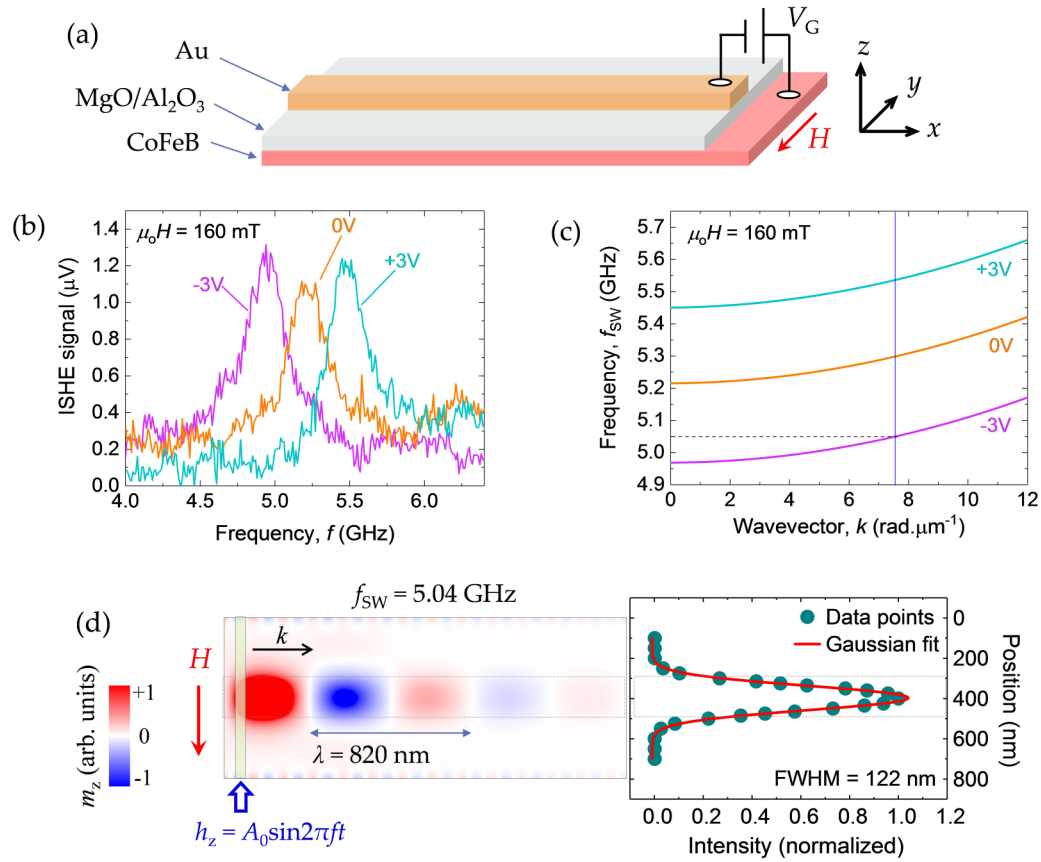

FIG. 5. (a) Schematic illustration of rectangular-shaped CoFeB film with a metal gate electrode on top of it. The DC gate voltage V_G is applied across the gate electrode and the film to create a virtual channel for SW propagation. (b) Experimental resonance spectra of the SWs measured at a bias magnetic field $\mu_0 H = 160\,\text{mT}$ for three values of V_G. (c) Analytical dispersion curves of the dipole-exchange SWs at $\mu_0 H = 160\,\text{mT}$ for three values of V_G. The solid vertical line represents the wave vector of the SWs excited using our nanoscale microwave antenna. The points at which this vertical line crosses the analytical curves give the SW frequency values for the three values of V_G. (d) Left panel: spatial map of the out-of-plane (z) component of the dynamic magnetization corresponding to the SW with $f_{SW} = 5.04\,\text{GHz}$ and $\lambda = 820\,\text{nm}$. Right panel: line scan (filled circles) of SW intensity along the rectangular film width at $x = 1\,\mu\text{m}$. The solid curve represents the fitting using a Gaussian function.

edges of the CoFeB film, thus ensuring that the relatively smaller components of the dynamic magnetization caused by the propagating SWs can be visualized easily under a background of uniform static magnetization. In Fig. 5(b), the resonance spectra of the experimentally measured SW signals from the 1.6-nm-thick CoFeB film at $\mu_0 H = 160\,\text{mT}$ are shown for three values of V_G. These resonance spectra show that the change in f_{SW} is approximately 265 MHz for $|V_G| =$ 3V, whereas the average FWHM value is about 300 MHz. This situation is similar to the situation at $\mu_0 H = 60\,\text{mT}$ in terms of the change in f_{SW} as compared to the FWHM value. In Fig. 5(c), the analytical SW dispersion curves at $\mu_0 H = 160\,\text{mT}$ are plotted using Eq. (4) for three different V_G values. These analytical curves also show a frequency shift of approximately 245 MHz at $k = 7.55\,\text{rad}\,\mu\text{m}^{-1}$ for $|V_G| = 3\text{V}$, which is very close to the experimentally observed frequency shift. In the simulations, the SWs are excited continuously by application of a sinusoidal magnetic field $h_z = \text{A}_0 \sin 2\pi f t$ of amplitude $A_0 = 0.5$ mT and frequency $f = 5.04\,\text{GHz}$. This sinusoidal field is applied to the film along the out-of-plane direction on the 50 nm × 800 nm rectangular area at a distance of 50 nm from the left edge of the rectangular film [Fig. 5(d)]. The frequency of the sinusoidal field is selected from the point at which the vertical line at $k = 7.55\,\text{rad}\,\mu\text{m}^{-1}$ crosses the dispersion curve for $V_G = -3\text{V}$ [see Fig. 5(c)]. The analytical curves indicate that the SWs with $f_{SW} = 5.04\,\text{GHz}$ and $k = 7.55\,\text{rad}\,\mu\text{m}^{-1}$, i.e., with $\lambda = 832\,\text{nm}$, can only be excited inside the NC, because SWs at this frequency are prohibited outside the NC. The spatial map of the out-of-plane component of the dynamic magnetization, as plotted in Fig. 5(d), shows that the excited SW with $\lambda = 820\,\text{nm}$ only propagates along the NC with a width ≈200 nm, although the sinusoidal magnetic field is applied across the entire rectangular film width. The line scan of the SW intensity along the width of the rectangular film at $x = 1\mu\text{m}$ is shown in the same figure. The Gaussian fitting (solid curve) shows that the FWHM is approximately 122 nm and that SW intensity drops by 77% (i.e., it becomes 23% of the peak value) at the edges of the NC when compared with the center of the NC. This confirms that the SWs are strictly confined inside the NC.

Finally, we calculate the decay length (L_d) of the SWs at $\mu_0 H = 160\,\text{mT}$ theoretically and compare the result with the simulation results. From the slope of the theoretical dispersion curve shown in Fig. 5(c), the group velocity (v_g) of the SWs

with $k = 7.55\,\text{rad}\,\mu\text{m}^{-1}$ can be calculated to be $132\,\text{m}\,\text{s}^{-1}$. By using Eq. (5) the SW decay length L_d, which is expressed as $L_d = v_g/\Gamma$, can be estimated to be 168 nm. We also extracted L_d from the simulation results. The extracted values of L_d are 220 and 530 nm for damping constants of 0.0247 and 0.01, respectively. This clearly shows that SWs with lower damping constants propagate for longer distances than SWs with higher damping constants. We mentioned earlier that the lower damping constant is selected in the simulations to allow the SWs to propagate for longer distances. Interestingly, the theoretical value of L_d is smaller than the simulated value. This is because, in the theory, point-like emitters and receivers are assumed, whereas in reality (i.e., in the experiments and simulations), these emitters and receivers both have finite sizes [37]. Furthermore, the inhomogeneous magnetization distribution in the vicinity of the film edges may also change the SW decay length relative to the calculated value.

IV. CONCLUSIONS

In summary, we have investigated electric field-based control of the UFMR and the dipole-exchange SWs in CoFeB films with three different thicknesses, which have iPMA. The SWs are excited electrically using a microwave antenna and are detected using spin pumping and the ISHE techniques. We have demonstrated control of the SW frequency via tuning of the iPMA of the CoFeB films by applying a gate voltage across the top gate electrode and the CoFeB films themselves. It was observed that the SW frequency was modified significantly by the VCMA, particularly, for the 1.6-nm-thick CoFeB film, in which the effective net anisotropy is reduced significantly by the iPMA. By performing micromagnetic simulations, we have demonstrated that an ultrathin ferromagnetic film with a lower effective net anisotropy is suitable for formation of virtual nanochannels (NCs) using VCMA; the dipole-exchange SWs can then be guided through these NCs, even though the VCMA coefficient is not very high. It should be mentioned here that the SWs in thicker films with higher effective net anisotropy values may also be guided through NCs produced by further increasing the VCMA coefficient. Several reports have shown that it is possible to increase the VCMA coefficient beyond $-70\,\text{fJ}\,\text{V}^{-1}\,\text{m}^{-1}$ for FM/oxide heterostructures [43,44]. In this report, we have only investigated control of the SW frequency using the VCMA. However, other properties of SWs, including their group velocity, decay length, and phase are also modulated by the VCMA at the same time. Further studies will be required to investigate the control of these properties of SWs.

ACKNOWLEDGMENTS

B.R. acknowledges Prof. Y. Fukuma for fruitful discussions. This work was supported by a Grant-in-Aid for Scientific Research on Innovative Area, "Nano Spin Conversion Science" (Grant No. 26103002). B.R. acknowledges RIKEN Incentive Research Project Grant No. FY2019. S.C. acknowledges the S. N. Bose National Centre for Basic Sciences for their financial assistance.

[1] T. Moriya, *Spin Fluctuations in Itinerant Electron Magnetism* (Springer-Verlag, Berlin, 1985).
[2] A. G. Gurevich and G. A. Melkov, *Magnetization Oscillations and Waves* (CRC Press, Boca Raton, Florida, 1996).
[3] D. D. Stancil and A. Prabhakar, *Spin Waves: Theory and Applications* (Springer, New York, 2008).
[4] A. Barman and J. Sinha, *Spin Dynamics and Damping in Ferromagnetic Thin Films and Nanostructures* (Springer, Cham, Switzerland, 2018).
[5] S. Neusser and D. Grundler, Magnonics: Spin waves on the nanoscale, Adv. Mater. **21**, 2927 (2009).
[6] V. V. Kruglyak, S. O. Demokritov, and D. Grundler, and Magnonics, J. Phys. D **43**, 260301 (2010).
[7] A. V. Chumak, V. I. Vasyuchka, A. A. Serga, and B. Hillebrands, Magnon spintronics, Nat. Phys. **11**, 453 (2015).
[8] T. Nozaki, Y. Shiota, S. Miwa, S. Murakami, F. Bonell, S. Ishibashi, H. Kubota, K. Yakushiji, T. Saruya, A. Fukushima, S. Yuasa, T. Shinjo, and Y. Suzuki, Electric-field-induced ferromagnetic resonance excitation in an ultrathin ferromagnetic metal layer, Nat. Phys. **8**, 491 (2012).
[9] B. Rana, Y. Fukuma, K. Miura, H. Takahashi, and Y. Otani, Excitation of coherent propagating spin waves in ultrathin CoFeB film by voltage-controlled magnetic anisotropy, Appl. Phys. Lett. **111**, 052404 (2017).
[10] Q. Wang, A. V. Chumak, L. Jin, H. Zhang, B. Hillebrands, and Z. Zhong, Voltage-controlled nanoscale reconfigurable magnonic crystal, Phys. Rev. B **95**, 134433 (2017).
[11] B. Rana and Y. Otani, Voltage-Controlled Reconfigurable Spin-Wave Nanochannels and Logic Devices, Phys. Rev. Appl. **9**, 014033 (2018).
[12] B. Rana and Y. Otani, Towards magnonic devices based on voltage-controlled magnetic anisotropy, Commun. Phys. **2**, 90 (2019).
[13] B. Dieny and M. Chshiev, Perpendicular magnetic anisotropy at transition metal/oxide interfaces and applications, Rev. Mod. Phys. **89**, 025008 (2017).
[14] Z.-P. Li, S. Li, Y. Zheng, J. Fang, L. Chen, L. Hong, and H. Wang, The study of origin of interfacial perpendicular magnetic anisotropy in ultra-thin CoFeB layer on the top of MgO based magnetic tunnel junction, Appl. Phys. Lett. **109**, 182403 (2016).
[15] S. Kanai, M. Tsujikawa, Y. Miura, M. Shirai, F. Matsukura, and H. Ohno, Magnetic anisotropy in Ta/CoFeB/MgO investigated by x-ray magnetic circular dichroism and first-principles calculation, Appl. Phys. Lett. **105**, 222409 (2014).
[16] H. X. Yang, M. Chshiev, B. Dieny, J. H. Lee, A. Manchon, and K. H. Shin, First-principles investigation of the very large perpendicular magnetic anisotropy at Fe/MgO and Co/MgO interfaces, Phys. Rev. B **84**, 054401 (2011).
[17] C. Duan, J. P. Velev, R. F. Sabirianov, Z. Zhu, J. Chu, S. S. Jaswal, and E. Y. Tsymbal, Surface Magnetoelectric Effect in Ferromagnetic Metal Films, Phys. Rev. Lett. **101**, 137201 (2008).
[18] T. Kawabe, K. Yoshikawa, M. Tsujikawa, T. Tsukahara, K. Nawaoka, Y. Kotani, K. Toyoki, M. Goto, M. Suzuki,

T. Nakamura, M. Shirai, Y. Suzuki, and S. Miwa, Electric-field-induced changes of magnetic moments and magnetocrystalline anisotropy in ultrathin cobalt films, Phys. Rev. B **96**, 220412 (2017).

[19] M. Tsujikawa and T. Oda, Finite Electric Field Effects in the Large Perpendicular Magnetic Anisotropy Surface Pt/Fe/Pt(001): A First-Principles Study, Phys. Rev. Lett. **102**, 247203 (2009).

[20] J. Zhu, J. A. Katine, G. E. Rowlands, Y. Chen, Z. Duan, J. G. Alzate, P. Upadhyaya, J. Langer, P. K. Amiri, K. L. Wang, and I. N. Krivorotov, Voltage-Induced Ferromagnetic Resonance in Magnetic Tunnel Junctions, Phys. Rev. Lett. **108**, 197203 (2012).

[21] R. Verba, V. Tiberkevich, I. Krivorotov, and A. Slavin, Parametric Excitation of Spin Waves by Voltage-Controlled Magnetic Anisotropy, Phys. Rev. Appl. **1**, 044006 (2014).

[22] Y.-J. Chen, H. K. Lee, R. Verba, J. A. Katine, I. Barsukov, V. Tiberkevich, J. Q. Xiao, A. N. Slavin, and I. N. Krivorotov, Parametric resonance of magnetization excited by electric field, Nano Lett. **17**, 572 (2017).

[23] B. Rana, Y. Fukuma, K. Miura, H. Takahashi, and Y. Otani, Effect of excitation power on voltage induced local magnetization dynamics in an ultrathin CoFeB film, Sci. Rep. **7**, 2318 (2017).

[24] M. Song, K.-W. Moon, C. Hwang, and K.-J. Kim, Omnidirectional Spin-Wave Array Antenna, Phys. Rev. Appl. **11**, 024027 (2019).

[25] K. Nawaoka, Y. Shiota, S. Miwa, H. Tomita, E. Tamura, N. Mizuochi, T. Shinjo, and Y. Suzuki, Voltage modulation of propagating spin waves in Fe, J. Appl. Phys. **117**, 17A905 (2015).

[26] T. Brächer, M. Fabre, T. Meyer, T. Fischer, S. Auffret, O. Boulle, U. Ebels, P. Pirro, and G. Gaudin, Detection of short-waved spin waves in individual microscopic spin-wave waveguides using the inverse spin Hall effect, Nano Lett. **17**, 7234 (2017).

[27] See Supplemental Material at http://link.aps.org/supplemental/10.1103/PhysRevB.100.224412 for: S1. Sample fabrication method, S2. Vibrating sample magnetometer (VSM) measurement of *M-H* curve of CoFeB films, S3. Anomalous Hall effect (AHE) measurment of CoFeB films, S4. Gate voltage dependence of SW frequencies, S5. Micromagnetic simulations.

[28] K. Ando, S. Takahashi, J. Ieda, Y. Kajiwara, H. Nakayama, T. Yoshino, K. Harii, Y. Fujikawa, M. Matsuo, S. Maekawa, and E. Saitoh, Inverse spin-Hall effect induced by spin pumping in metallic system, J. Appl. Phys. **109**, 103913 (2011).

[29] L. Chen, M. Decker, M. Kronseder, R. Islinger, M. Gmitra, D. Schuh, D. Bougeard, J. Fabian, D. Weiss, and C. H. Back, Robust spin-orbit torque and spin-galvanic effect at the Fe/GaAs (001) interface at room temperature, Nat. Commun. **7**, 13802 (2016).

[30] L. Liu, T. Moriyama, D. C. Ralph, and R. A. Buhrman, Spin-Torque Ferromagnetic Resonance Induced by the Spin Hall Effect, Phys. Rev. Lett. **106**, 036601 (2011).

[31] K. Kondou, H. Sukegawa, S. Mitani, K. Tsukagoshi, and S. Kasai, Evaluation of spin Hall angle and spin diffusion length by using spin current-induced ferromagnetic resonance, Appl. Phys. Express **5**, 073002 (2012).

[32] G. Carlotti and G. Gubbiotti, Brillouin scattering and magnetic excitations in layered structures, Riv. Nuovo. Cimento. **22**, 1 (1999).

[33] S. Kasai, K. Kondou, H. Sukegawa, S. Mitani, K. Tsukagoshi, and Y. Otani, Modulation of effective damping constant using spin Hall effect, Appl. Phys. Lett. **104**, 092408 (2014).

[34] S. Ikeda, K. Miura, H. Yamamoto, K. Mizunuma, H. D. Gan, M. Endo, S. Kanai, J. Hayakawa, F. Matsukura, and H. Ohno, A perpendicular-anisotropy CoFeB–MgO magnetic tunnel junction, Nat. Mater. **9**, 721 (2010).

[35] S. Pal, B. Rana, O. Hellwig, T. Thomson, and A. Barman, Tunable magnonic frequency and damping in $[Co/Pd]_8$ multilayers with variable Co layer thickness, Appl. Phys. Lett. **98**, 082501 (2011).

[36] A. Okada, S. Kanai, M. Yamanouchi, S. Ikeda, F. Matsukura, and H. Ohno, Electric-field effects on magnetic anisotropy and damping constant in Ta/CoFeB/MgO investigated by ferromagnetic resonance, Appl. Phys. Lett. **105**, 052415 (2014).

[37] V. Vlaminck and M. Bailleul, Spin-wave transduction at the submicrometer scale: Experiment and modeling, Phys. Rev. B **81**, 014425 (2010).

[38] B. A. Kalinikos and A. N. Slavin, Theory of dipole-exchange spin wave spectrum for ferromagnetic films with mixed exchange boundary conditions, J. Phys. C **19**, 7013 (1986).

[39] H. Ulrichs, B. Lenk, and M. Münzenberg, Magnonic spin-wave modes in CoFeB antidot lattices, Appl. Phys. Lett. **97**, 092506 (2010).

[40] O. Mosendz, J. E. Pearson, F. Y. Fradin, G. E. W. Bauer, S. D. Bader, and A. Hoffmann, Quantifying Spin Hall Angles from Spin Pumping: Experiments and Theory, Phys. Rev. Lett. **104**, 046601 (2010).

[41] V. E. Demidov, M. P. Kostylev, K. Rott, P. Krzysteczko, G. Reiss, and S. O. Demokritov, Generation of the second harmonic by spin waves propagating in microscopic stripes, Phys. Rev. B **83**, 054408 (2011).

[42] M. J. Donahue and D. G. Porter, OOMMF User's Guide, Version 1.0, Interagency Report NISTIR 6376, National Institute of Standards and Technology, Gaithersburg, MD (Sept 1999), http://math.nist.gov/oommf/.

[43] S. Miwa, J. Fujimoto, P. Risius, K. Nawaoka, M. Goto, and Y. Suzuki, Strong Bias Effect on Voltage-Driven Torque at Epitaxial Fe-MgO Interface, Phys. Rev. X **7**, 031018 (2017).

[44] A. Kozioł-Rachwał, T. Nozaki, K. Freindl, J. Korecki, S. Yuasa, and Y. Suzuki, Enhancement of perpendicular magnetic anisotropy and its electric field-induced change through interface engineering in Cr/Fe/MgO, Sci. Rep. **7**, 5993 (2017).